

## Embedded graphene for large-area silicon-based devices

M. A. Gluba,<sup>a)</sup> D. Amkreutz, G. V. Troppenz, J. Rappich, and N. H. Nickel

*Institut für Silizium-Photovoltaik, Helmholtz-Zentrum Berlin für Materialien und Energie GmbH, Kekuléstraße 5, 12489 Berlin, Germany*

(Received 29 May 2013; accepted 28 July 2013; published online 12 August 2013)

Macroscopic graphene films buried below amorphous and crystalline silicon capping layers are studied by Raman backscattering spectroscopy and Hall-effect measurements. The graphene films are grown by chemical vapor deposition on copper foil and transferred to glass substrates. Uncapped films possess charge-carrier mobilities of  $2030 \text{ cm}^2/\text{Vs}$  at hole concentrations of  $3.6 \times 10^{12} \text{ cm}^{-2}$ . Graphene withstands the deposition and subsequent crystallization of silicon capping layers. However, the crystallinity of the silicon cap has large influence on the field-induced doping of graphene. Temperature dependent Hall-effect measurements reveal that the mobility of embedded graphene is limited by charged-impurity and phonon-assisted scattering. © 2013 AIP Publishing LLC.

[<http://dx.doi.org/10.1063/1.4818461>]

Fundamental studies on the charge-carrier transport in graphene mainly focus on small flakes obtained by micromechanical cleavage (MMC) of highly ordered pyrolytic graphite.<sup>1–3</sup> Carbon monolayers produced by this technique were reported to possess carrier mobilities of up to  $44.000 \text{ cm}^2/\text{Vs}$ . However, only small non-contiguous sheets with lateral dimensions of a few micrometers can be produced. The MMC technique is thus unsuited for large area devices such as solar cells and flat panel displays, where homogeneous graphene films with dimensions ranging from a few square centimeters to square meters are required.

On the other hand, chemical vapor deposition (CVD) is evolving as an efficient route to wafer-scale graphene fabrication.<sup>4–6</sup> The lateral dimensions of the resulting graphene layers are limited only by the size of the available furnace.<sup>7</sup> However, the grain structure of these large area graphene films and hence the charge transport therein differs considerably from graphene flakes obtained by micromechanical cleavage. Since the metal substrates for CVD growth are neither single crystalline nor lattice-matched, the resulting graphene films are polycrystalline and accumulate a large amount of strain during the growth.<sup>8</sup>

Recently, buried graphene electrodes were demonstrated in GaN-based light-emitting diodes by Kim *et al.*<sup>9</sup> The conductive performance of the electrodes improved drastically when a cap of silicon nitride ( $\text{SiN}_x$ ) was applied on top of the graphene layer. This improvement was solely attributed to the protection of graphene against oxidation. In contrast, the impact of fixed charges, typically contained in  $\text{SiN}_x$  films, on the charge-carrier balance of the buried graphene electrodes was not discussed.

Despite the desire to implement graphene into silicon-based device structures, there is a substantial lack of knowledge concerning charge transport and scattering mechanisms of charge carriers in embedded graphene. In this work, we investigate the impact of electron-beam deposition and crystallization of silicon capping layers on the electronic properties of embedded graphene. Using Raman-backscattering and temperature dependent Hall-effect measurements, we

show that charge transport in buried graphene is governed by impurity and phonon-assisted scattering mechanisms.

Macroscopic graphene layers were produced by catalytic decomposition of methane on copper foil within a CVD process.<sup>4</sup> Prior to the growth, the copper substrates were cleaned in an ultrasonic bath of acetone and isopropyl alcohol. Surface oxides were removed by dipping the copper in acetic acid. In order to study their electrical and optical properties, the graphene layers were transferred to transparent and non-conducting Corning Eagle borosilicate glass substrates using a standard polymer-assisted transfer process.

The graphene sheets were characterized by micro-Raman backscattering spectroscopy using the 633 nm line of a focused HeNe-laser. The scattered light is dispersed in a grating monochromator which offers a resolution better than  $1 \text{ cm}^{-1}$ . Due to the polycrystalline nature of the copper substrates and inhomogeneous strain in the graphene films, the frequency of phonon modes differs considerably along the surface. In order to reliably characterize the films, 10 measurements at different positions on each sample were performed and evaluated statistically.

Electrical characterization was performed with Hall-effect measurements. A van-der-Pauw geometry of ohmic contacts was prepared by applying conductive silver paint to the edges of the graphene film. The dimension of the probed layers amounted to about  $8 \times 8 \text{ mm}^2$ .

To study the influence of a capping layer on the charge carrier transport in embedded graphene, some of the samples were coated with 300 nm amorphous silicon (a-Si) by electron-beam deposition from a 6N Si target at a process pressure of  $10^{-7} \text{ mbar}$  and a temperature of  $200^\circ\text{C}$ . The Si layers were eventually crystallized by scanning a high-energy electron beam over the surface. The energy introduced during the crystallization process was varied between 500 and  $725 \text{ mJ/mm}^2$  at a draw rate of  $6 \text{ mm/s}$ . Reference samples prepared with the same process but without underlying graphene exhibit negligible electric conductance. Hence, the electric characteristics of the graphene/Si layer stack are solely determined by the graphene layer.

Raman spectra of the CVD-grown graphene are depicted in Figure 1. The characteristic phonon modes are well

<sup>a)</sup>Electronic mail: marc.gluba@helmholtz-berlin.de

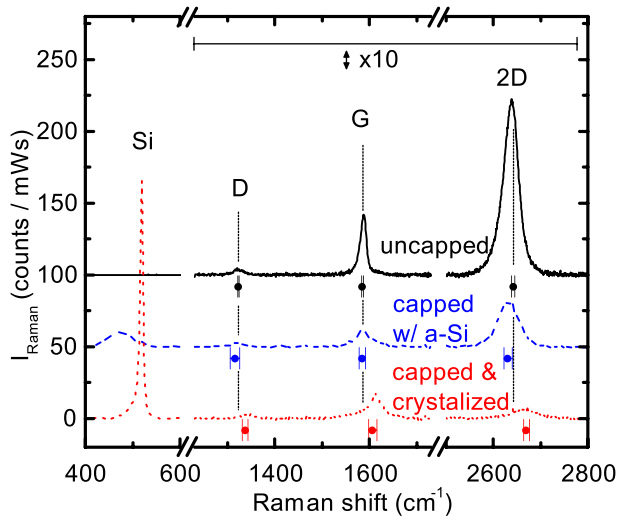


FIG. 1. Characteristic Raman spectra of bare graphene on glass, capped with amorphous, and post-crystallized silicon. Data points and error bars indicate mean Raman shift and standard deviation obtained from different positions on the sample. For clarity, the spectra are shifted vertically and the graphene part is magnified by a factor of 10.

observed in the spectrum of uncapped graphene transferred to the Corning Eagle borosilicate glass substrate (solid line in Fig. 1). Although the graphene layer underwent the chemically and mechanically demanding transfer process, the defect related D mode at  $1323\text{ cm}^{-1}$  is less pronounced than the lattice vibrations of the G and 2D modes at  $1585$  and  $2642\text{ cm}^{-1}$ , respectively. This indicates that the graphene film withstands the chemical stress during dissolution of the copper substrate and the mechanical stress due to the flexibility of the supporting polymer. The ratio of the 2D to G Raman modes of bare graphene transferred onto the glass substrate amounts to 2.9. This value is comparable to results commonly obtained for single layer graphene on the chemically related silicon oxide substrate.<sup>10</sup>

To determine the homogeneity of large area graphene, the phonon frequencies were measured at different positions on the sample. In case of bare graphene on glass, the standard deviation amounts to 1.8, 1.8, and  $3.2\text{ cm}^{-1}$  for the D, G, and 2D phonon modes, respectively (Table I). This shows that the transfer process onto glass substrates results in graphene films of pronounced homogeneity.

Interestingly, the characteristic Raman spectrum is preserved when a-Si is deposited onto the graphene layer (dashed line in Fig. 1). Besides the D, G, and 2D modes of graphene, the phonon mode of a-Si is observed at  $474\text{ cm}^{-1}$ . The presence of the a-Si layer causes a pronounced decrease of the intensity of the graphene related phonon modes. This decrease is not caused by damage of the graphene layer,

since the intensity of the defect sensitive D mode is still very low. In fact, the lower intensity of the spectrum is due to optical absorption of the a-Si layer through which the phonon modes of the embedded graphene were measured. Furthermore, the ratio of the 2D to G Raman modes amounts to 2.4, which is similar to the ratio obtained for uncapped graphene. This clearly demonstrates that the structure of embedded graphene is not affected by the deposition of the a-Si capping layer.

The a-Si capping layer was crystallized using an electron beam. A subsequent Raman measurement revealed that the embedded graphene endured the crystallization procedure. The dotted line in Figure 1 shows the D, G, and 2D modes of the corresponding phonon spectrum. Compared to graphene embedded in a-Si, the lower ratio of the 2D to G phonon mode of 0.4 either indicates an increase in damage of the graphene film or a deviation from the intrinsic charge carrier balance due to the crystallization treatment. It is important to note that the low intensity ratio is not caused by multilayer graphene, since all graphene layers stem from the same growth cycle. Since the crystallization process involves temperature gradients larger than  $300\text{ K/mm}$ , electron-beam crystallization makes high demands on the thermal and structural stability of embedded graphene. Despite these rough conditions, the characteristic Raman spectrum of graphene is still detectable after the crystallization process clearly demonstrating that the embedded graphene layer survives the deposition and crystallization process of the silicon capping layer. Moreover, the standard deviation of the Raman frequencies is similar to or even lower than that of graphene embedded in amorphous silicon (Table I).

When graphene is covered with an a-Si or poly-Si layer, the frequencies of the phonon modes shift by up to  $27\text{ cm}^{-1}$ . Amorphous Si deposited onto the graphene layer results in a shift to lower frequencies by 6.9, 0.6, and  $11.4\text{ cm}^{-1}$  for the D, G, and 2D phonon modes, respectively. A shift to higher frequencies of the D, G, and 2D phonon modes by 14.2, 21.4, and  $27.4\text{ cm}^{-1}$  is observed after crystallization of the a-Si capping layer (Table I). The variation of the phonon frequencies of embedded graphene can be caused by (i) mechanical strain due to volume shrinkage of the Si matrix during crystallization,<sup>11</sup> and (ii) by field-effect doping induced by fixed charges at the graphene interfaces.<sup>12</sup>

To elucidate the origin of the observed deviation from the phonon frequencies of bare graphene, Hall-effect measurements were performed. Figure 2 shows the temperature dependence of the Hall-effect mobility, charge carrier density, and sheet resistance of bare and embedded graphene. The as-transferred layer exhibits hole conduction with a carrier mobility of about  $\mu = 2070\text{ cm}^2/\text{Vs}$ , which varies only slightly with temperature [open diamonds in Fig. 2(a)]. Due to the polycrystalline nature of CVD graphene, the macroscopic mobility is lower compared to values commonly reported for micro-mechanically cleaved graphene flakes. On the other hand, our data are consistent with field-effect mobilities reported for CVD graphene.<sup>4-6</sup> However, it is important to note that the sample area used in our investigations is 5 to 6 orders of magnitude larger and hence, the impact of grain boundaries and other lateral singularities on the charge transport is raised.

TABLE I. Mean frequency  $\bar{\nu}$  and standard deviation  $\sigma$  of the D, G, and 2D phonon modes of bare and embedded graphene.

	$\bar{\nu}_D$ ( $\text{cm}^{-1}$ )	$\sigma_D$ ( $\text{cm}^{-1}$ )	$\bar{\nu}_G$ ( $\text{cm}^{-1}$ )	$\sigma_G$ ( $\text{cm}^{-1}$ )	$\bar{\nu}_{2D}$ ( $\text{cm}^{-1}$ )	$\sigma_{2D}$ ( $\text{cm}^{-1}$ )
Bare graphene	1322.8	1.8	1585.2	1.8	2642.2	3.2
Capped w/a-Si	1315.9	10.1	1584.6	6.7	2630.8	8.7
Capped and crystallized	1337.0	6.3	1606.6	8.8	2669.6	6.1

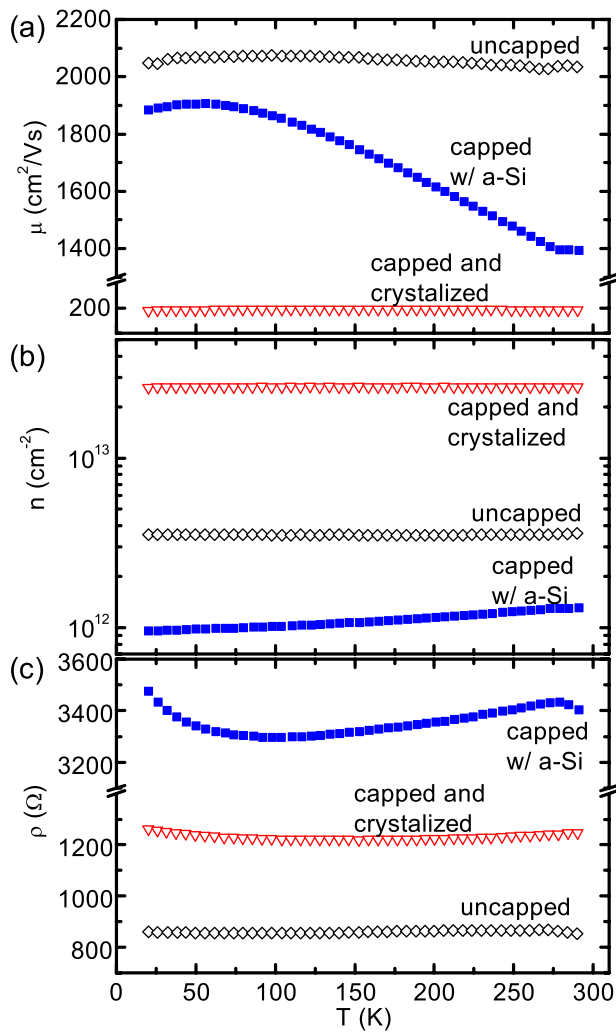


FIG. 2. Temperature dependence of (a) Hall mobility, (b) charge carrier density, and (c) sheet resistance of bare graphene on a glass, capped with amorphous, and post-crystallized silicon. Open and closed symbols denote hole and electron conduction, respectively.

While the electrical characteristics of uncapped graphene hardly depend on temperature, the mobility of graphene capped with a-Si exhibits a strong temperature dependence [solid squares in Fig. 2(a)]. As the temperature increases from 20 K towards 300 K, the mobility increases and reaches a maximum value of  $1906 \text{ cm}^2/\text{Vs}$  at around  $T = 56 \text{ K}$ . Then  $\mu$  decreases and reaches a value of  $1393 \text{ cm}^2/\text{Vs}$  at 300 K. Interestingly, the deposition of the a-Si capping layer causes carrier-type conversion from holes to electrons. Moreover, the carrier density decreases by about a factor of 3 to  $n = 1.1 \times 10^{12} \text{ cm}^{-2}$  compared to the uncapped graphene layer. The changes of the Hall mobility are accompanied by a linear increase of the electron concentration from  $9.5 \times 10^{11} \text{ cm}^{-2}$  at 20 K to  $1.3 \times 10^{12} \text{ cm}^{-2}$  at 300 K [solid squares in Fig. 2(b)].

Electron-beam crystallization of the Si capping layer causes a second type conversion. For graphene embedded in poly-Si, the majority carriers are holes similar to the exposed film. During the crystallization process, the Hall mobility in the graphene layer decreases by one order of magnitude to a value of  $190 \text{ cm}^2/\text{Vs}$  at 300 K. This is accompanied by an increase of the hole concentration by one order of

magnitude. The observed decrease of the Hall mobility and increase of the carrier concentration indicates that enhanced ionized impurity scattering dominates the charge transport for embedded graphene after crystallization of the Si capping layer [open triangles in Figs. 2(a) and 2(b)] as will be discussed later. The reduction of the Hall mobility and the increase of the carrier concentration compensate to some extent. Nonetheless, the resulting sheet resistance of the poly-Si capped graphene layer of  $1247 \Omega$  is about 30% larger than that of bare graphene [Fig. 2(c)]. Our results clearly demonstrate that graphene can be utilized as an active layer covered by amorphous and polycrystalline silicon. Most likely, this attribute of graphene is not limited to silicon and its deposition conditions.

Since monolayer graphene is exceptionally thin, interactions with the substrate and with layers on its surface, such as a-Si and poly-Si, strongly affect its physical properties. Particularly, localized electric fields influence charge carrier balance and phonon scattering. Moreover, the electronic and the vibrational systems are effectively coupled by a Kohn anomaly in the phonon dispersion.<sup>13,14</sup> Consequently, the Raman transitions are sensitive to charge-carrier type and concentration. Fundamental insight into charge-carrier transport is obtained from Raman backscattering spectroscopy and Hall-effect measurements. These methods provide complementary data to elucidate underlying microscopic mechanisms on charge transport.

A theoretical study on the influence of the charge-carrier concentration on the lattice dynamics in graphene was reported by Lazzeri *et al.*<sup>15</sup> They investigated the frequency shift of the G mode by applying time-dependent second-order perturbation theory. The calculations predict an asymmetric frequency shift of the G mode where the shift caused by hole doping exceeds that of electron doping. Based on these calculations and the carrier concentrations measured in the differently embedded graphene layers, a shift of the G mode frequency of  $\nu_{\text{capped}} - \nu_{\text{bare}} \approx -5.5$  and  $+16 \text{ cm}^{-1}$  is expected for graphene covered with a-Si and poly-Si, respectively. These values are in qualitative agreement with the frequency shift of  $-1$  and  $+21 \text{ cm}^{-1}$ , we observed experimentally (Fig. 1). The frequency shift caused by changing the charge carriers can be masked by compressive strain. The difference of about  $5 \text{ cm}^{-1}$  between measured and anticipated G mode frequency could thus be ascribed to compressive strain which accumulates during cool down of the samples after the deposition of amorphous Si. The average strain sensitivity<sup>16–18</sup> of graphene of  $65 \text{ cm}^{-1}/\%$  and the residual frequency shift of about  $5 \text{ cm}^{-1}$  imply a compressive strain of 0.08%. This strain compares well to the value of 0.1% which would be introduced by the difference in the thermal expansion coefficients if the graphene perfectly followed the contraction of the a-Si cap from  $200^\circ\text{C}$  to room temperature.

Interestingly, the frequency of the G mode,  $\nu_{\text{bare}}$ , of bare graphene on glass is already influenced by hole accumulation and hence, it differs from the intrinsic frequency of isolated graphene by about  $2 \text{ cm}^{-1}$ . The hole conduction can be caused by polymer or etchant residues or by field-induced doping from fixed charges in the glass substrate. Capping the graphene layer with a-Si compensates these effects resulting

in a lower charge carrier concentration compared to the poly-Si capped and bare graphene layers. Moreover, embedding graphene in a-Si could probably improve the device characteristics of graphene-based field-effect transistors (GFETs). Current devices suffer from high threshold voltages which are caused by unintentional carrier accumulation. Embedding the active graphene channel into a-Si could lower its charge-carrier concentration and thus retune the Fermi energy towards the charge neutrality point to reduce the threshold voltage of GFETs.

The impact of field-effect doping on Raman transitions is not restricted to the zone-center G mode. A similar effect was observed for the 2D mode by Das *et al.*<sup>19</sup> in Raman measurements performed on top-gated field-effect transistors. Our data show that a field-induced shift can also be observed for the defect related D mode. Graphene capped with a-Si exhibits a shift of  $v_{\text{capped}} - v_{\text{bare}} = -7$  and  $-11 \text{ cm}^{-1}$  for the D and 2D modes, respectively. For graphene capped with poly-Si this shift becomes positive and amounts to  $v_{\text{capped}} - v_{\text{bare}} = +14$  and  $+28 \text{ cm}^{-1}$ . The 2D Raman transition involves inelastic scattering at two phonons with opposing wave vectors of the K-point of the Brillouin zone. In contrast, for the D mode, one of those scattering events is exchanged by elastic scattering at a lattice defect.<sup>20</sup> Consequently, the field-induced shift of the D-mode is exactly half the shift of the 2D mode which is consistent with the experimental data.

The crystallinity of the silicon capping layer influences the charge transport in the embedded graphene. While the transport characteristics of a-Si capped graphene depend strongly on temperature, carrier concentration, and mobility in the post-crystallized samples show only very weak temperature dependence (see Fig. 2). Moreover, the majority carrier-type changes from electron- to hole-conduction due to the crystallization process. This hitherto unreported behavior is a direct consequence of field-induced doping by an increased concentration of charges protruding into the buried graphene layer. During the crystallization process, a vast amount of negatively charged centers, including oxygen- and boron-induced charge traps,<sup>21</sup> Pb-centers,<sup>22</sup> and extrinsic impurities from the glass substrate, are created at the interface or diffuse there with the help of excess heat from the crystallization process.

The dominant scattering mechanisms of the charge carrier transport in bare graphene are still debated. Possible limitations include remote interfacial phonon-scattering and classical mechanisms such as impurity scattering.<sup>23,24</sup> To analyze the transport governing mechanisms in the a-Si embedded graphene layers, we evaluate the mobility data of a-Si capped graphene in Figure 3 on a double logarithmic scale. The presence of a maximum of the mobility vs. temperature plot indicates that two competing microscopic mechanisms limit the charge transport in different temperature regimes. A simple model comprising two independent processes of the form  $\mu_{1,2} \sim T^{\gamma_{1,2}}$  can account for the experimental data. The individual mobilities contribute to the measured value according to Matthiessen's rule as  $\mu = \mu_1 \mu_2 / (\mu_1 + \mu_2)$ . A fit of the model to the data shown in Fig. 3 yields the exponents:  $\gamma_1 = 0.04$  and  $\gamma_2 = -1.71$  for the different scattering mechanisms (dashed and dotted lines in Fig. 3). Moreover, using

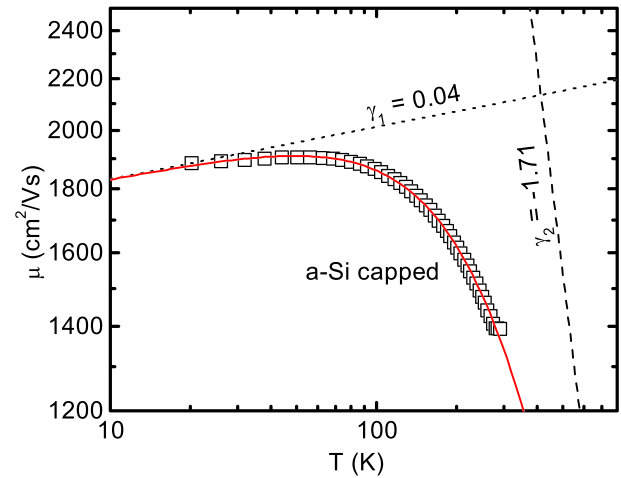


FIG. 3. Temperature dependence of the charge-carrier mobility of graphene embedded in a-Si. The dashed and dotted lines represent scattering processes of the form  $\mu_{1,2} \sim T^{\gamma_{1,2}}$ . The solid line represents a fit with  $\gamma_1 = 0.04$  and  $\gamma_2 = -1.71$ .

the linear dependence of the charge-carrier density on temperature the individual mobility  $\mu_1$  translates into the conductivity  $\sigma_1 = ne\mu_1 \sim n^{\gamma_1+1}$ . A linear relation of conductivity and carrier concentration implying  $\gamma_1 \approx 0$  is typically found for graphene-based field-effect devices. This is commonly attributed to charged impurity scattering.<sup>24</sup> Hence, at low temperatures, the mobility of a-Si capped graphene is limited by coulomb scattering at charged impurities.

At  $T > 50 \text{ K}$ , a steep decrease of  $\mu$  is observed. The corresponding temperature exponent of  $\gamma_2 = -1.71$  is consistent with phonon scattering in conventional non-polar semiconductors.<sup>25</sup> Hence, our data clearly demonstrate that charge carrier transport at high temperatures is governed by phonon-assisted scattering. It is important to note that this scattering process limits the mobility in a-Si embedded graphene at room temperature and thus, might be a limiting mechanism for large area graphene-based applications such as solar cells and touch screen displays.

In summary, Raman backscattering experiments have shown, that the characteristic properties of graphene persist after deposition and crystallization of silicon capping layers. Although these demanding process conditions do not cause substantial damage to the graphene film, they have a considerable impact on the electronic properties. Raman and Hall-effect measurements reveal a drastic change of the field-effect doping of graphene embedded in a-Si and post-crystallized poly-Si. In contrast to the commonly observed hole conduction, the electric current in graphene embedded in a-Si is mediated by electrons. Eventually, hole conduction is restored by post-crystallizing the amorphous silicon cap. Moreover, crystallization fosters the field-effect doping in embedded graphene. On the one hand, this leads to reduced carrier mobility due to increased coulomb scattering, but on the other hand raises the carrier concentration by an order of magnitude. Consequently, the sheet resistance of a graphene layer embedded in a poly-Si device is comparable to that of bare graphene.

This work has been supported by the European Union through the EFRE program (ProFIT grant, Contract No. 10147374).



- <sup>1</sup>K. S. Novoselov, A. K. Geim, S. V. Morozov, D. Jiang, Y. Zhang, S. V. Dubonos, I. V. Grigorieva, and A. A. Firsov, *Science* **306**, 666 (2004).
- <sup>2</sup>E. V. Castro, H. Ochoa, M. I. Katsnelson, R. Gorbachev, D. C. Elias, K. S. Novoselov, A. K. Geim, and F. Guinea, *Phys. Rev. Lett.* **105**, 266601 (2010).
- <sup>3</sup>X. Du, I. Skachko, A. Barker, and E. Y. Andrei, *Nat. Nanotechnol.* **3**, 491 (2008).
- <sup>4</sup>X. Li, W. Cai, J. An, S. Kim, J. Nah, D. Yang, R. Piner, A. Velamakanni, I. Jung, E. Tutuc, S. K. Banerjee, L. Colombo, and R. S. Ruoff, *Science* **324**, 1312 (2009).
- <sup>5</sup>W. Liu, H. Li, C. Xu, Y. Khatami, and K. Banerjee, *Carbon* **49**, 4122 (2011).
- <sup>6</sup>S. Lee, K. Lee, and Z. Zhong, *Nano Lett.* **10**, 4702 (2010).
- <sup>7</sup>S. Bae, H. Kim, Y. Lee, X. Xu, J.-S. Park, Y. Zheng, J. Balakrishnan, T. Lei, H. R. Kim, Y. I. Song, Y.-J. Kim, K. S. Kim, B. Özyilmaz, J.-H. Ahn, B. H. Hong, and S. Iijima, *Nat. Nanotechnol.* **5**, 574 (2010).
- <sup>8</sup>R. He, L. Zhao, N. Petrone, K. S. Kim, M. Roth, J. Hone, P. Kim, A. Pasupathy, and A. Pinczuk, *Nano Lett.* **12**, 2408 (2012).
- <sup>9</sup>B.-J. Kim, C. Lee, M. A. Mastro, J. K. Hite, C. R. Eddy, Jr., F. Ren, S. J. Pearton, and J. Kim, *Appl. Phys. Lett.* **101**, 031108 (2012).
- <sup>10</sup>A. C. Ferrari, J. C. Meyer, V. Scardaci, C. Casiraghi, M. Lazzeri, F. Mauri, S. Piscanec, D. Jiang, K. S. Novoselov, S. Roth, and A. K. Geim, *Phys. Rev. Lett.* **97**, 187401 (2006).
- <sup>11</sup>N. Nakanishi, H. Arie, Y. Kunitune, T. Ide, Y. Hirose, N. Hattori, and T. Koyama, *J. Appl. Phys.* **112**, 043518 (2012).
- <sup>12</sup>S. Pisana, M. Lazzeri, C. Casiraghi, K. S. Novoselov, A. K. Geim, A. C. Ferrari, and F. Mauri, *Nature Mater.* **6**, 198 (2007).
- <sup>13</sup>W. Kohn, *Phys. Rev. Lett.* **2**, 393 (1959).
- <sup>14</sup>S. Piscanec, M. Lazzeri, M. Mauri, A. C. Ferrari, and J. Robertson, *Phys. Rev. Lett.* **93**, 185503 (2004).
- <sup>15</sup>M. Lazzeri and F. Mauri, *Phys. Rev. Lett.* **97**, 266407 (2006).
- <sup>16</sup>C. Metzger, S. Remi, M. K. Liu, S. V. Kusminskiy, A. H. C. Neto, A. K. Swan, and B. B. Goldberg, *Nano Lett.* **10**, 6 (2010).
- <sup>17</sup>F. Ding, H. X. Ji, Y. H. Chen, A. Herklotz, K. Dorr, Y. F. Mei, A. Rastelli, and O. G. Schmidt, *Nano Lett.* **10**, 3453 (2010).
- <sup>18</sup>Y. C. Cheng, Z. Y. Zhu, G. S. Huang, and U. Schwingenschlöggl, *Phys. Rev. B* **83**, 115449 (2011).
- <sup>19</sup>A. Das, S. Pisana, B. Chakraborty, S. Piscanec, S. K. Saha, U. V. Waghmare, K. S. Novoselov, H. R. Krishnamurthy, A. K. Geim, A. C. Ferrari, and A. K. Sood, *Nat. Nanotechnol.* **3**, 210 (2008).
- <sup>20</sup>M. S. Dresselhaus, G. Dresselhaus, R. Saito, and A. Jorio, *Phys. Rep.* **409**, 47 (2005).
- <sup>21</sup>H. Park, B. Choi, A. Steigerwald, K. Varga, and N. Tolk, *J. Appl. Phys.* **113**, 023711 (2013).
- <sup>22</sup>G. J. Gerardi, E. H. Poindexter, P. J. Caplan, and N. M. Johnson, *Appl. Phys. Lett.* **49**, 348 (1986).
- <sup>23</sup>J.-H. Chen, C. Jang, S. Xiao, M. Ishigami, and M. S. Fuhrer, *Nat. Nanotechnol.* **3**, 206 (2008).
- <sup>24</sup>J.-H. Chen, C. Jang, S. Adam, M. S. Fuhrer, E. D. Williams, and M. Ishigami, *Nat. Phys.* **4**, 377 (2008).
- <sup>25</sup>J. Bardeen and W. Shockley, *Phys. Rev.* **80**, 72 (1950).